

## Article

# A Numerical Investigation of Supercavitation Vehicle's Hydrodynamic Noise

Jiacheng Ye, Jing Zhang , Yuebing Wang and Peng Zhao 

Key Laboratory of Acoustics Research, College of Metrology and Measurement Engineering,  
China Jiliang University, Hangzhou 310018, China; p21020854140@cjl.u.edu.cn (J.Y.)

\* Correspondence: 19a0205127@cjl.u.edu.cn

**Abstract:** This paper presents the simulation results of the acoustic field around an underwater supercavitation vehicle under various operating conditions and analyzes the cavitation phenomenon and the hydrodynamic noise spectrum. Regarding the ventilated cavitation phenomenon, the simulation shows that low vehicle speed can reduce the threshold of the ventilated supercavitation, and high background pressure can enhance the stability of the supercavitation structure. As for hydrodynamic noise, firstly, the simulation results reveal that when cavitation occurs, the noise spectrum exhibits several characteristic peaks near 1 kHz and between 3 and 10 kHz. The overall noise amplitude demonstrates a descending trend between 10 and 40 kHz. Further, under natural cavitation conditions, a characteristic peak is detectable between 40 and 80 kHz. The influence of the operating conditions on the noise is essentially achieved by altering the scale of the cavitation flow: with the growth of the bubble flow scale, the noise between 3 and 10 kHz first increases and then decreases due to its own pulsation and the masking effect, while the noise between 10 to 40 kHz substantially reduces. On the other hand, if the scale expansion of bubble flow is related to the increase of ventilation flow, the noise amplitude near 1 kHz will increase significantly. These results provide theoretical support for studying the supercavitation vehicles' noise and applying the ventilated supercavitation technology.

**Keywords:** hydrodynamic noise; supercavitation; ventilated cavitation



**Citation:** Ye, J.; Zhang, J.; Wang, Y.; Zhao, P. A Numerical Investigation of Supercavitation Vehicle's Hydrodynamic Noise. *J. Mar. Sci. Eng.* **2023**, *11*, 1004. <https://doi.org/10.3390/jmse11051004>

Academic Editor: Alon Gany

Received: 13 April 2023

Revised: 1 May 2023

Accepted: 6 May 2023

Published: 8 May 2023



**Copyright:** © 2023 by the authors. Licensee MDPI, Basel, Switzerland. This article is an open access article distributed under the terms and conditions of the Creative Commons Attribution (CC BY) license (<https://creativecommons.org/licenses/by/4.0/>).

## 1. Introduction

Cavitation is a phenomenon in which the local pressure of a liquid drops to the saturation vapor pressure and causes the formation and evolution of cavitation bubbles. Its mechanism is mainly related to the accumulation and dissipation of energy in the local area [1,2]. For instance, on the surface of a high-speed underwater vehicle, the deposition of kinetic energy facilitates a water pressure drop and the cavitation phenomenon can occur. Investigators commonly employ non-dimensional cavitation numbers to measure the development of the cavitation phenomenon on the vehicle surface by calculating the ratio of the potential energy of fluid pressure to kinetic energy per unit volume. However, it should be noted that the scale of the cavitation bubble cluster and cavitation intensity are not equivalent. Varga [3] and De [4] suggested that the cavitation number determines the scale of the cavitation bubble cluster, while the cavitation intensity is chiefly related to the cavitation noise. The research by Liu et al. [5] and Rabiee et al. [6] indicates that cavitation intensity initially lessens and then increases with the growth of the bubble cluster.

When the cavitation is sufficiently developed, the bubble cluster surrounds the vehicle and the vehicle sails in the cavitation flow [2,7], and it can be considered that supercavitation occurs. The evolution of supercavitation flow involves multiple processes of closure and separation [8]. Jiang et al. [9], Mohammadrahimi et al. [10], and Shao et al. [11] independently examined supercavitation vehicle models with different head shapes and concluded that the cone-shaped head design is desirable to form the stable supercavitation. Based on

their work, Pham et al. [12] tested several models with conical heads of various angles and found that smaller cone angles contribute to the occurrence of supercavitation. After supercavitation occurs, the drag force experienced by the vehicle is substantially reduced. Hence, supercavitation technology has been extensively used to reduce underwater vehicle drag. However, due to the unsteady characteristics of the natural supercavitation and also in order to enhance the drag reduction efficiency, researchers have developed ventilated cavitation technology. This technique discharges gas to the vehicle's surface to achieve ventilated supercavitation. Considering that the bubble clusters on the vehicle's surface could disrupt communication with the external environment and generate significant noise, it is imperative to research the noise caused by the underwater supercavitation vehicle.

Noise caused by underwater vehicles primarily includes mechanical noise generated by the vibration of mechanical structures and hydrodynamic noise generated by water flow radiation. In the case of no cavitation bubble in the flow field, the higher the sailing speed and the deeper the sailing depth, the higher the noise amplitude [13]. Nevertheless, through the occurrence of cavitation, the cavitation bubble cluster becomes the main source of hydrodynamic noise. In natural cavitation conditions, the collapse of cavitation bubbles and pressure fluctuations at the gas–liquid interface generate substantial noise, and under ventilation conditions, the jet from vent to supercavitation structures also generates noticeable noise [14–16]. The complex mechanism of cavitation bubble cluster collapse and its pressure wave propagation makes it difficult to establish a supercavitation noise model [17,18]. Zhang et al. [19] employed a single-bubble collapse acoustic model to simulate supercavitation radiation noise, whereas Skidmore et al. [20] developed a correlation between noise and pressure distribution inside the supercavitation. Under ventilation conditions, Gilbert et al. [16] infer that the gas–liquid interface behaves like a quarter-wave resonator. Although there are some discrepancies between the results of these models and the experimental results, they provide theoretical support for noise reduction technology by changing the position of the vent to reduce noise radiation [15] and adjusting the ventilation frequency away from the frequency of cavitation vibration to avoid resonance [20,21].

Regarding the noise characteristics of a supercavitation vehicle, the cavitation noise exhibits continuous spectrum characteristics. Recently, Yasui's [22] research has shown that fluctuating the number of bubbles in the bubble cluster can cause broadband noise. Tu et al. [13], Skidmore et al. [20], and Nouri et al. [23] independently discovered in their water tunnel experiments that the cavitation noise could have prominent dipole characteristics. Nouri et al. [23] also found that when supercavitation occurs, the noise exhibits unipolar features. In general, research on supercavitation vehicle noise characteristics is currently lacking and mainly focuses on the low-frequency range [14,15]. It is attributed to the broad radiation spectrum and the high noise level of low-frequency domain noise.

This paper employed a conical-headed vehicle model to examine the operating conditions required for supercavitation and its relevant hydrodynamic noise over a broader frequency range of 100 Hz to 100 kHz. Our research aims to fill the current gap about the ventilated supercavitation vehicle and its hydrodynamic noise.

## 2. Numerical Method

In the current paper, the LES is utilized to investigate the flow field. The Schnerr–Sauer cavitation model and the VOF method simulate the two-phase flow and depict the interface between the two phases. The FW-H unsteady model is used to solve the acoustic signal.

### 2.1. Governing Equations

The background flow field of the supercavitation vehicle is a typical gas–liquid two-phase flow field. Under ventilated conditions, the gas is taken as non-condensable air. Therefore, the flow field consists of three components: the water component, cavitation component, and ventilated air component, and the total volume fraction of the constituent components is equal to (1) [24].

$$\alpha_1 + \alpha_2 + \alpha_3 = 1 \quad (1)$$

where  $\alpha$  is the phase volume fraction. In the following parts, subscripts 1, 2, 3 denote the water component, cavitation component, and ventilated air component, respectively.

The governing equations of the flow field include the mass conservation equation, the momentum conservation equation, the cavitation model equation, and the inter-phase transport equation.

The mass conservation equation reads:

$$\frac{\partial \rho}{\partial t} + \frac{\partial(\rho u_i)}{\partial x_i} = 0 \quad (2)$$

$$\rho = \sum_{n=1}^3 \alpha_n \rho_n \quad (3)$$

where  $\rho$  denotes the density of the mixed fluid and  $u_i$  represents the velocity component of the mixed fluid in the  $i$  direction. In the following parts, subscripts  $i, j$ , and  $k$  all denote the directions of the Cartesian coordinate system.

The momentum conservation equation is expressed by:

$$\frac{\partial(\rho u_i)}{\partial t} + \frac{\partial(\rho u_i u_j)}{\partial x_i} = \rho g_i - \frac{\partial p}{\partial x_i} + \frac{\partial \tau_{ij}}{\partial x_j} \quad (4)$$

$$\tau_{ij} = \mu \left( \frac{\partial u_i}{\partial x_j} + \frac{\partial u_j}{\partial x_i} - \frac{2}{3} \delta_{ij} \frac{\partial u_k}{\partial x_k} \right) \quad (5)$$

$$\mu = \sum_{n=1}^3 \alpha_n \mu_n \quad (6)$$

where  $g_i$  signifies the component of the gravitational acceleration in the  $i$ -th direction,  $\tau_{ij}$  represents the viscous stress,  $\mu$  denotes the dynamic viscosity of the mixed fluid. Further,  $\delta_{ij}$  is the Kronecker delta symbol (when  $i = j$ ,  $\delta_{ij} = 1$ ; when  $i \neq j$ ,  $\delta_{ij} = 0$ ).

The simulation adopts the Schnerr–Sauer cavitation model [25], which is based on the Rayleigh–Plesset simplified equation and neglects the effects of viscosity and surface tension. This model has been widely used in numerical simulations for cavitation noise prediction and its accuracy in predicting cavitation phenomena has been experimentally verified. The specific form of the Schnerr–Sauer cavitation model is as follows:

$$\frac{dR}{dt} = \sqrt{\frac{2}{3} \left( \frac{p_{sat} - p}{\rho_1} \right)} \quad (7)$$

in which  $R$  represents the radius of the cavitation bubble,  $p_{sat}$  is the saturated vapor pressure, and  $p$  denotes the pressure of the water around the bubble.

The phase transition process of the cavitation model is commonly controlled by the interphase transport equation, as its specific form is provided by the following relation:

$$\frac{\partial(\alpha_2 \rho_2)}{\partial t} + \frac{\partial(\alpha_2 \rho_2 u_j)}{\partial x_j} = S_{\alpha n} = S_{Re} - S_{Rc} \quad (8)$$

$$S_{Re} = \frac{\rho_1 \rho_2}{\rho} \alpha_1 \alpha_2 \frac{3}{R} \sqrt{\frac{2}{3} \frac{P - P_v}{\rho_1}}, P \leq P_v \quad (9)$$

$$S_{Rc} = \frac{\rho_1 \rho_2}{\rho} \alpha_1 \alpha_2 \frac{3}{R} \sqrt{\frac{2}{3} \frac{P_v - P}{\rho_1}}, P \geq P_v \quad (10)$$

where  $S_{mn}$ ,  $S_{Re}$ , and,  $S_{Rc}$  signify the mass source item, condensation source item, and evaporation source item, respectively.

## 2.2. Acoustic Model

The hydrodynamic noise of a supercavitation vehicle is a typical far-field noise generated by the flow, and the FW-H acoustic integral formula is the preferred strategy for predicting far-field noise. It calculates the far-field sound signal from near-field fluid data to predict sound pressure fluctuations. So we adopted the FW-H acoustic model and the Lighthill stress tensor model to integrate the sound radiation data on the FW-H surface and the FW-H domain and evaluate the sound pressure fluctuations at the point receiver.

The FW-H equation is given by,

$$P'_T(\mathbf{x}, T) = \frac{1}{4\pi} \left\{ \int_{(f=0)} \left[ \frac{\rho v_n [r \dot{M}_r] + a_0 (M_r - M^2)}{r^2 (1 - M_r)^3} \right] dS \right\}_{ret} \quad (11)$$

$$P'_L(\mathbf{x}, T) = \frac{1}{4\pi} \left\{ \frac{1}{a_0} \int_{(f=0)} \left[ \frac{\dot{L}_i r_i}{r(1 - M_r)^2} \right] dS + \int_{(f=0)} \left[ \frac{L_r - L_i M_i}{r(1 - M_r)^2} \right] dS + \frac{1}{a_0} \int_{(f=0)} \left[ \frac{L_r [r \dot{M}_r + a_0 (M_r - M^2)]}{r^2 (1 - M_r)^3} \right] dS \right\}_{ret} \quad (12)$$

where  $P'_T(\mathbf{x}, T)$  is the monopole term and  $P'_L(\mathbf{x}, T)$  is the dipole term.  $T$  represents the spectrum analysis time,  $v_n$  is the normal velocity of the integral surface, and  $r_i$  denotes the distance between the point receiver and the sound source.  $a_0$  is the sound speed in quiescent medium. In addition,  $M_r$  signifies the Mach number of the source towards the point receiver,  $S$  corresponds to the FW-H integral surface and the subscript *ret* stands for the time that sound radiation is emitted (i.e., the difference between the times of noise generation and reception).

As for the quadrupole noise source term, it involves volume integration over the source field, and its particular form is as follows:

$$p'_Q(\mathbf{x}, T) = \frac{1}{4\pi} \left\{ \left( \frac{1}{c} \right) \left( \frac{\partial^2}{\partial t^2} \right) \int_{-\infty}^t \left[ \int_{(f>0)} \frac{T_{rr}}{r} d\Omega \right] d\tau + \left( \frac{\partial}{\partial t} \right) \int_{-\infty}^t \left[ \int_{(f>0)} \frac{3T_{rr} - T_{ii}}{r^2} d\Omega \right] d\tau \right\} + \left\{ c \int_{-\infty}^t \left[ \int_{(f>0)} \frac{3T_{rr} - T_{ii}}{r^3} d\Omega \right] d\tau \right\} \quad (13)$$

where  $d\Omega$  is the element of surface area of the collapsing sphere  $g = 0$  ( $g = \tau_t + r/c$ ).  $T_{rr}$  represents the double contraction of the Lighthill stress tensor ( $T_{ij}$ ),  $r_i$  denotes the component of the unit vector in the radiation direction, and  $\tau$  is the source time.

## 2.3. Calculation Approach

Calculations basically implement an implicit unsteady method. The maximum target frequency in our research on different conditions is in the range of 100 Hz to 100 kHz, hence, the minimum time step is set to  $5 \times 10^{-6}$  s. The convection term is discretized using a second-order upwind scheme in space. A segregated flow solver based on a simple algorithm is exploited to solve the coupled velocity and pressure problem. The VOF multiphase flow model employs a second-order implicit scheme to solve and utilizes the HRIC method to capture the details of the multiphase flow field.

## 3. Numerical Simulation Set-Up

### 3.1. Vehicle Model

The numerical study employed a supercavitation vehicle model, as demonstrated in Figures 1 and 2. The model consists of the cavitator and the main body part. The cavitator part is a cone with a base edge length of 132 mm and a cone angle of  $36^\circ$ , whereas the main

body part is 2100 mm in length and has a maximum diameter of 180 mm. The vent is only present in the model for the ventilation condition, and its width is 20 mm.

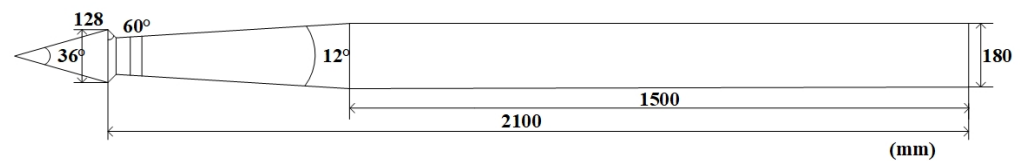


**Figure 1.** Schematic representation of the vehicle model with its dimensions.

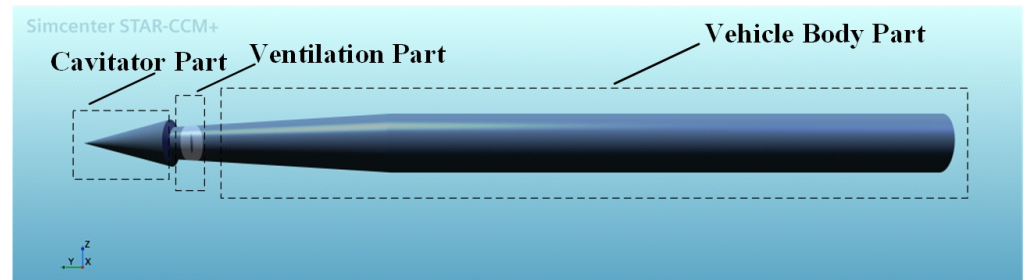


**Figure 2.** The structural diagram of the vehicle model.

### 3.2. The Wall Boundary Setting and Mesh Partitioning

The computational domain is presented in Figure 3, where the flow velocity at the velocity inlet is controlled to simulate the vehicle velocity. The pressure outlet is set at the boundaries around the vehicle to simulate the diving depth. Under natural cavitation conditions, the vehicle surface is assumed as the solid wall, and under ventilated cavitation conditions, the vent is set as the mass flow inlet to realize ventilation. It should be noted that the ventilation flow direction is normal to the surface of the vehicle.

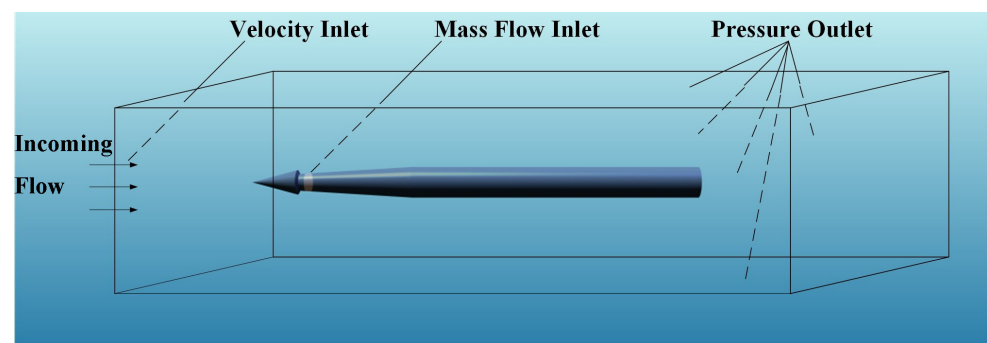


**Figure 3.** Schematic representation of the wall boundary settings.

Both the FW-H method and the LES model have high requirements for the computational mesh, and ventilation also exacerbates the unsteady characteristics of the flow field. Therefore, after experimental research, as demonstrated in Figure 4, the trimmed mesh is utilized in the whole computational domain, with a mesh of multi-layered prism layers on the FW-H surface and the vehicle's surface. The mesh near the surface and in the wake area of the vehicle is densified with several layers. The element number of mesh in the computational domain is approximately 28,000,000.

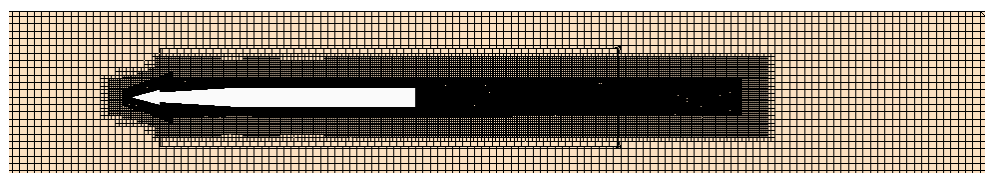


**Figure 4.** Mesh partitioning diagram.

### 3.3. Noise Source and Point Receiver Setting

In order to check that the cavitation flow is the main source of the hydrodynamic noise after cavitation occurs, as shown in Figure 5, the noise source should be divided into two parts: the noise source of the cone part and the noise source of the cavitation flow part. The hydrodynamic noise of the cone part is mainly related to the pressure fluctuation caused by the incoming flow impacting the cavitator. On the other hand, the noise of the cavitation flow part primarily includes the pressure wave generated by the collapse of cavitation bubbles, pressure fluctuations inside the bubble flow caused by ventilation, bubble flow pulsation caused by the increase or decrease in the number of the bubbles in the bubble cluster, pressure fluctuations around the cavitation flow caused by the shedding of the cavitation flow, and noise generated by the fragmentation of ventilated air in the wake, etc.

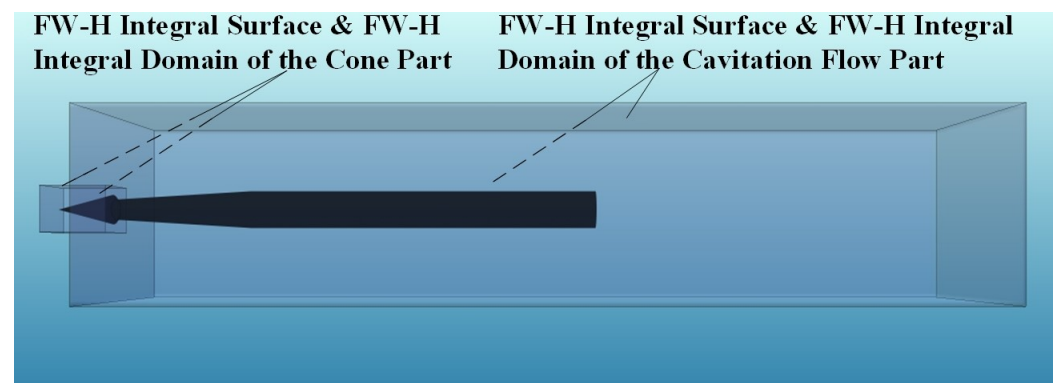


**Figure 5.** FW-H integral surface and integral domain setting diagram.

As demonstrated in Figure 6, the point receiver is arranged on the cavitator, and the corresponding coordinate is considered as (0.12 m, −0.2 m, 0.12 m). Experimental investigation indicates that the noise data received by the point receiver located in the same vertical plane and at the same distance as transmitted vertically to the vehicle's surface are basically the same. Additionally, in the X–Z vertical plane, when the point receiver is closer to the vehicle's surface, each time the point receiver moves 0.06 m away from the vehicle, the received full-frequency noise data are reduced by 3 dB on average.

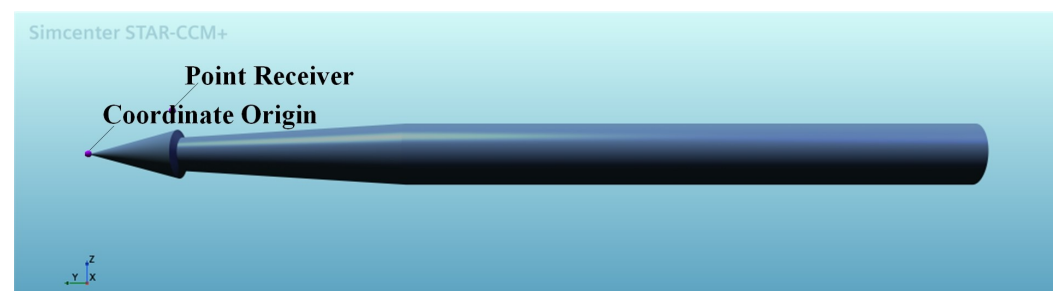


**Figure 6.** Noise point receiver position setting diagram.

## 4. Results and Discussion

This section focuses on cavitation phenomena and hydrodynamic noise under multiple operating conditions, including natural cavitation in the low-pressure and low-velocity experimental environments, ventilated cavitation in the low-pressure and low-velocity experimental environments, natural cavitation in the high-pressure and high-velocity practical environments, and ventilated cavitation in the high-pressure and high-velocity practical environments. In continuing, the effects of vehicle speed, flow field background pressure, ventilation status, and ventilation flow on the hydrodynamic noise in the flow field and the cavitation phenomena in the vehicle's surface are methodically examined.

The noise data processing utilized FFT, the amplitude function is set to sound pressure level, while the frequency function is set to frequency, and we did not use filters and window



functions. The reference sound pressure level is  $1 \times 10^{-6}$  Pa, which is the commonly used reference sound pressure in the field of underwater acoustics for processing noise signals. Multiple sets of acoustic pressure wave data received by the point receiver under different operating conditions were analyzed, the time domain signals are converted to frequency domain signals, and the spectrum diagram is then drawn. The measurement of the cavitation phenomenon mainly employs the natural cavitation number and ventilation rate [26], and we also provided the thickness and length of the cavitation flow on the vehicle surface and the proportional of various components in the cavitation flow.

The calculation formulas of natural cavitation number and ventilation rate are as follows,

$$\sigma = \frac{p_0 - p_v}{\frac{1}{2}\rho_1 v^2} \quad (14)$$

$$C_q = \frac{Q/\rho_3}{v_\infty D_n^2} \quad (15)$$

where  $\sigma$  denotes the natural cavitation number, which is a dimensionless parameter to measure the occurrence and development of cavitation in natural cavitation conditions.  $C_q$  denotes the ventilation rate, which is a dimensionless parameter to measure the occurrence and development of ventilated cavitation in ventilated cavitation conditions. It should be noted that both parameters are affected by multiple factors, such as flow geometry, viscosity, surface tension, and cavitation nucleus content. So when using these two dimensionless parameters in the research, it is also necessary to combine the specific analysis of the scale of the cavitation flow in the flow field.  $p_v$  represents the saturated vapor pressure of water,  $\rho_1 = 997 \text{ kg/m}^3$  is the density of water,  $\rho_3 = 1.18 \text{ kg/m}^3$  is the density of ventilated air,  $v$  stands for the speed of the incoming flow,  $Q$  signifies the ventilation mass flow, and  $D_n = 0.18 \text{ m}$  is the diameter of the vehicle's cylindrical part.

#### 4.1. Cavitation Phenomenon under Different Operating Conditions

In the numerical research, multiple cases of four different types and several operating conditions are utilized. For each case, the specific operating conditions, such as the vehicle's velocity, the diving depth, and the ventilated flow; the cavitation phenomena in the flow field includes the contour of the volume fraction of each phase in the flow field and the length and thickness of the cavitation flow on vehicle's surface; the value of the dimensionless parameter namely the natural cavitation number and the ventilated rate, for cavitation and ventilated cavitation; and the corresponding time step used in the simulation, are taken as follows. Firstly, we conducted a comparative study on multiple different cases in which natural cavitation occurs under low-pressure and low-velocity conditions.

As illustrated in Figure 7 and Table 1 mentioned above, the comparison of Case 1, Case 2, and Case 3 reveals that achieving natural supercavitation in a water tunnel environment requires tight control of the background pressure in the flow domain or ensuring a very high incoming flow velocity. However, in general, the current water tunnel equipment could provide only the incoming flow velocity below 20 m/s and background pressure above 0.1 atm. Therefore, it is difficult to achieve natural supercavitation in the water tunnel experiment.

**Table 1.** The parameters of the natural cavitation condition in the experimental environment.

Case	Vehicle Speed (m/s)	Background Pressure (atm)	Cavitation Number	Cavitation Flow's Length (m)	Cavitation Flow's Thickness (m)	Time Step ( $\mu$ s)
1	10.00	0.04	$1.03 \times 10^{-2}$	4.83	0.13	50
2	15.00	0.05	$1.36 \times 10^{-2}$	3.70	0.11	5
3	20.00	0.10	$3.31 \times 10^{-2}$	2.01	0.06	50

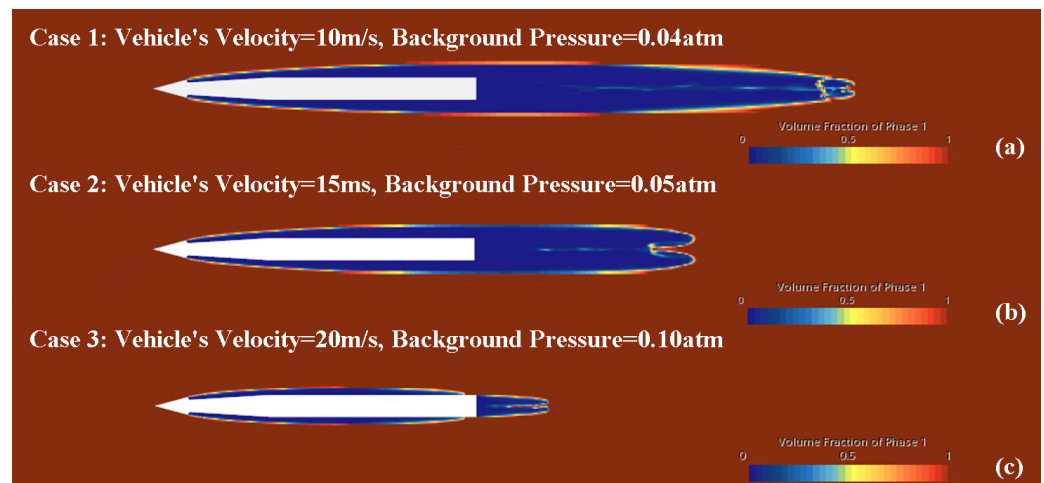


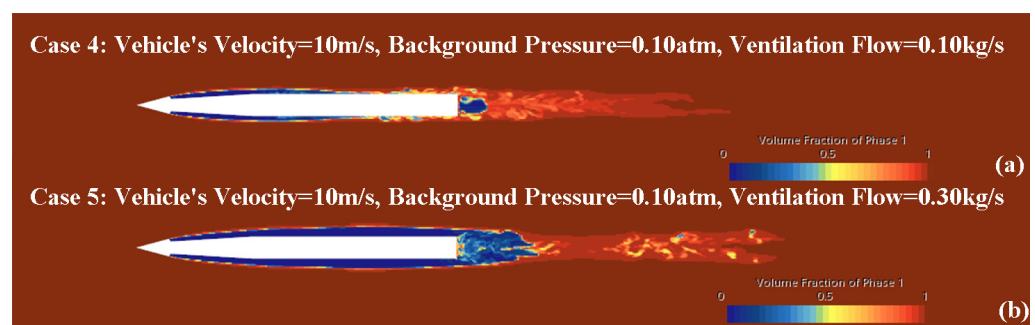
**Figure 7.** Contour plots of the liquid phase volume fraction, where natural cavitation occurs in the experimental environment, including: (a) Case 1, (b) Case 2, (c) Case 3.

As demonstrated in Figure 8 and Table 2, under the ventilated condition, with the ventilation flow increases, the vehicle's surface is first covered by a thin layer of air film, which we refer to as the air film. When the ventilation flow rate increases several times, the bubble flow at the shoulder and the wake of the vehicle begin to merge, which we call critical supercavitation. Furthermore, when the ventilation flow increases significantly again, the bubble flow at the shoulder and wake of the vehicle complete merger, referred to as ventilated supercavitation.

**Table 2.** The parameters of the ventilated cavitation in the experimental environment.

Case	Vehicle's Speed (m/s)	Background Pressure (atm)	Cavitation Number	Ventilation Flow (kg/s)	Ventilation Rate	Cavitation Flow's Length (m)	Cavitation Flow's Thickness (m)	Time Step ( $\mu$ s)
4	10.00	0.10	$1.32 \times 10^{-1}$	0.10	$2.62 \times 10^{-1}$	1.40	0.04	50
5	10.00	0.10	$1.32 \times 10^{-1}$	0.30	$7.85 \times 10^{-1}$	2.65	0.07	5

As illustrated in Figure 9 and Table 3 mentioned above, comparing Case 6 and Case 7 shows that the cavitation number in Equation (4) may differ from the actual occurrence and development of cavitation, and when the vehicle speed is not high enough, even if the vehicle is near the water surface, it is still difficult to achieve natural supercavitation in practical environments.

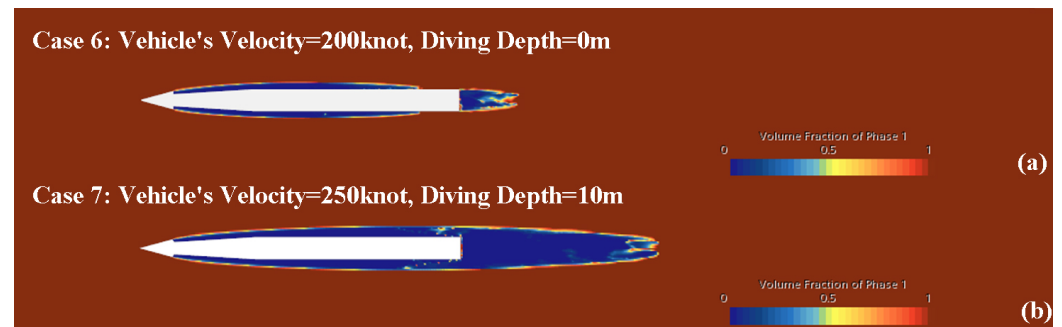


**Figure 8.** Contour plots of the liquid phase volume fraction, where ventilated cavitation occurs in the experimental environment, including: (a) Case 4, (b) Case 5.



**Table 3.** The parameters of the natural cavitation condition in the practical environment.

Case	Vehicle's Speed (knot)	Diving Depth (m)	Cavitation Number	Cavitation Flow's Length (m)	Cavitation Flow's Thickness (m)	Time Step ( $\mu$ s)
6	200.00	0.00	$1.85 \times 10^{-2}$	1.81	0.05	10
7	250.00	10.00	$2.37 \times 10^{-2}$	3.51	0.10	5

**Figure 9.** Contour plots of the liquid phase volume fraction, where the natural cavitation occurs in the practical environment, including: (a) Case 6, (b) Case 7.

In order to investigate the effect of background pressure, other conditions are kept fixed, and compare different cases under various diving depths. Referring to Table 4 and Figure 10, Case 10, Case 13, and Case 16 are selected, where their diving depths are 5, 10, and 20 m, respectively, the vehicle velocity is set as 180 knot, and the ventilation flow is set as 0.8 kg/s. As demonstrated in Figure 10c,f,i, the cavitation flow in the shoulder and wake of the vehicle is merging, and the ventilated flow is in the critical supercavitation stage. In Case 10, the ventilated cavitation flow scale is larger, but it has a higher proportion of liquid phase. In Case 13, the ventilated cavitation flow scale lessens, and the liquid phase in the bubble flow decreases. In Case 16, the ventilated cavitation flow scale is smaller, and the proportion of liquid is even lower. Therefore, it can be concluded that diving depth affects the scale of ventilated cavitation flow on the vehicle's surface when critical supercavitation occurs but basically does not affect the threshold of ventilated supercavitation. Furthermore, when critical ventilated supercavitation occurs, the low background pressure may reduce the stability of the internal structure in the ventilated cavitation flow. Then, by increasing the ventilation flow to 1.2 kg/s, as illustrated in Figure 10d,g,j, the complete ventilated supercavitation structures are present in the flow field. By observing Table 4, it can be seen that after forming a complete supercavitation structure, a deeper diving depth results in a longer supercavitation flow length, opposite to the effect of diving depth on supercavitation flow length during the critical supercavitation.

Figure 11 shows the volume fraction of the ventilated air component in the flow field after the solution becomes stable. It can be seen that the ventilated air does not cover the vehicle but configures a thin layer of air film slightly away from the vehicle's surface. Meanwhile, the vapor component repeatedly undergoes shedding and generation processes during the solver iteration and cannot reach stability. The interface between the ventilated air and the cavitation component is confused. So it is unsuitable for research. As a result, controlling the natural cavitation number at a high value to make the flow field essentially comprises no cavitation component is necessary to study ventilated supercavitation.

From the calculation formula of the ventilation rate in Equation (4), it is easy to see that the vehicle velocity affects the ventilated cavitation flow's scale. Choose a position where the diving depth is 20 m, and the ventilation flow is 0.8 kg/s. In Case 8, the vehicle speed is 160 knots, and a complete supercavitation structure is observed in the flow field, as demonstrated in Figure 10a. In Case 16, the vehicle speed increases up to 180 knots, and as shown in Figure 10i, the bubble flow is in the critical supercavitation state. In Case 19, the vehicle speeds up to 200 knots, as presented in Figure 10k, and only a layer of air film is

detectable on the vehicle's surface. Therefore, it can be concluded that the vehicle speed substantially affects the threshold of ventilated supercavitation. The lower the vehicle speed, the easier it is to achieve ventilated supercavitation, which corresponds to the velocity term in the ventilation rate formula. Increasing the ventilation flow to 1.2 kg/s, as illustrated in Figure 10b,j,i, the complete ventilated supercavitation structure exists in the flow field. In Case 9, the vehicle speed is the lowest, and the length of the ventilated supercavitation flow is the longest. In contrast, the supercavitation flow scale is the shortest in Case 20, with the highest vehicle speed. This indicates that the vehicle speed affects the threshold of ventilated supercavitation and the scale of the ventilated cavitation flow. In ventilation conditions, the lower the vehicle speed, the larger the scale of the ventilated supercavitation flow on the vehicle's surface.

**Table 4.** The parameters of the ventilated cavitation in the practical environment.

Case	Vehicle's Speed (m/s)	Diving Depth (m)	Cavitation Number	Ventilation Flow (kg/s)	Ventilation Rate	Cavitation Flow's Length (m)	Cavitation Flow's Thickness (m)	Time Step ( $\mu$ s)
8	160.00	20	$8.68 \times 10^{-2}$	0.80	$2.54 \times 10^{-1}$	2.78	0.07	5
9	160	20	$8.68 \times 10^{-2}$	1.20	$3.81 \times 10^{-1}$	4.49	0.12	5
10	180	5	$3.43 \times 10^{-2}$	0.80	$2.26 \times 10^{-1}$	2.81	0.07	5
11	180	5	$3.43 \times 10^{-2}$	1.20	$3.39 \times 10^{-1}$	2.74	0.07	5
12	180	15	$5.72 \times 10^{-2}$	0.40	$1.13 \times 10^{-1}$	1.58	0.04	10
13	180	15	$5.72 \times 10^{-2}$	0.80	$2.26 \times 10^{-1}$	2.58	0.07	5
14	180	15	$5.72 \times 10^{-2}$	1.20	$3.39 \times 10^{-1}$	3.07	0.08	5
15	180	20	$6.86 \times 10^{-2}$	0.40	$1.13 \times 10^{-1}$	1.06	0.04	5
16	180	20	$6.86 \times 10^{-2}$	0.80	$2.26 \times 10^{-1}$	2.46	0.07	5
17	180	20	$6.86 \times 10^{-2}$	1.20	$3.39 \times 10^{-1}$	3.41	0.10	5
18	200	0	$1.85 \times 10^{-2}$	0.60	$1.53 \times 10^{-1}$			20
19	200	20	$5.56 \times 10^{-2}$	0.80	$2.03 \times 10^{-1}$	1.24	0.04	5
20	200	20	$5.56 \times 10^{-2}$	1.20	$3.05 \times 10^{-1}$	2.73	0.07	5

Note: In Case 18, the gas-liquid interface is unstable and the components of the cavitation flow could not stabilize, thus the length and thickness of the cavitation flow are not measured.

Moreover, considering the effect of ventilation flow on the ventilated cavitation phenomenon, it is easy to infer that higher ventilation flow leads to a larger length of ventilation flow and is more likely to lead to ventilation supercavitation. This speculation is confirmed by Figure 10h,i,j. Furthermore, comparing Cases 15–17 shows that a stable air film can form on the vehicle's surface under relatively low ventilation conditions, and the ventilated supercavitation requires several times more ventilation flow.

#### 4.2. Noise Sources and Noise Order Characteristics

In order to check that the flow around the supercavitation vehicle is the main source of hydrodynamic noise after cavitation occurs, the hydrodynamic noise from the cone part of the vehicle and the cavitation flow part should be distinctly examined. As demonstrated in Figure 12, the hydrodynamic noise from the cone section is mainly related to the pressure fluctuations caused by the incoming flow impinging on the cavitator. On the other hand, the noise from the cavitation flow part mostly includes the pulsations and shedding of the cavitation flow, and the pressure fluctuation caused by the ventilation.

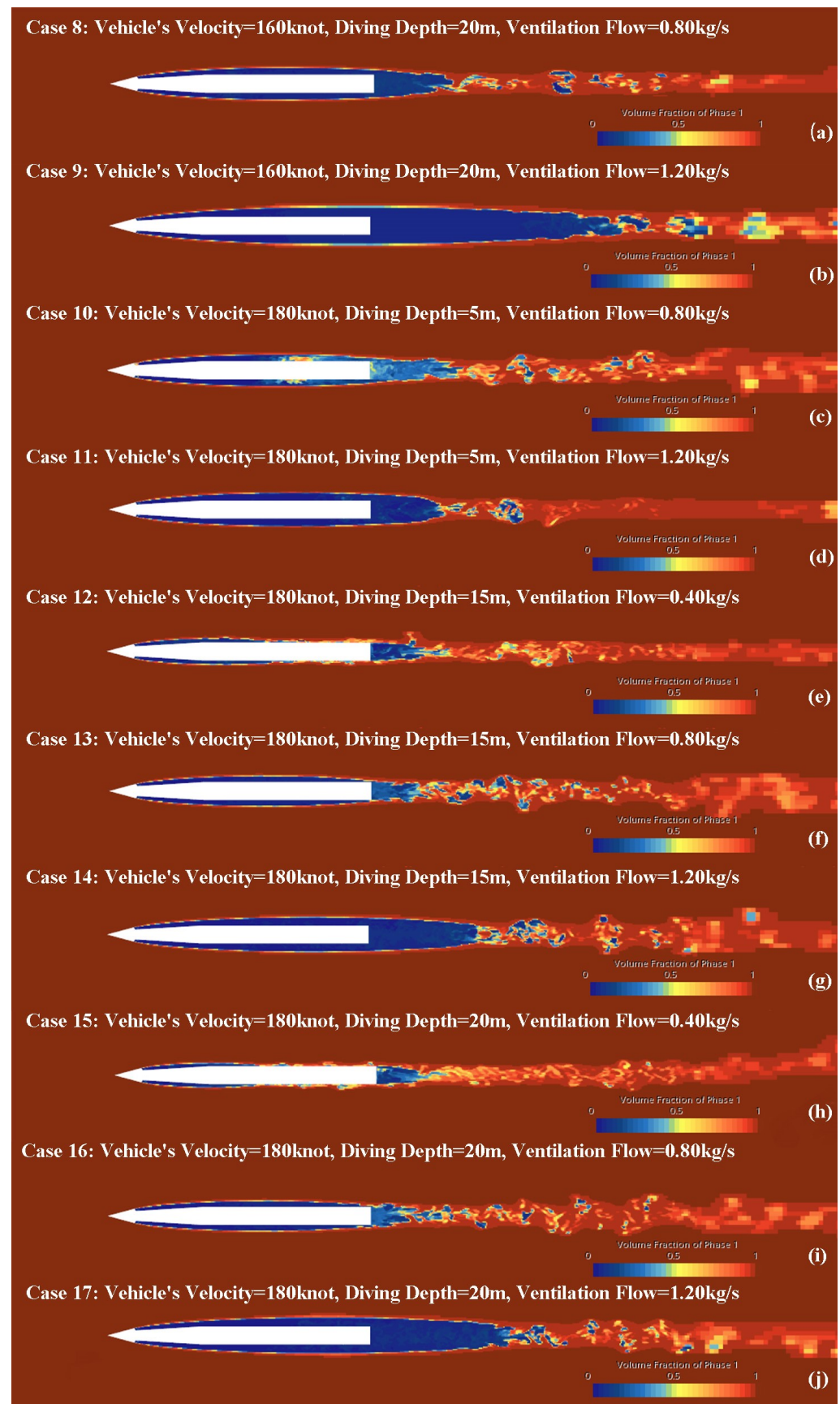
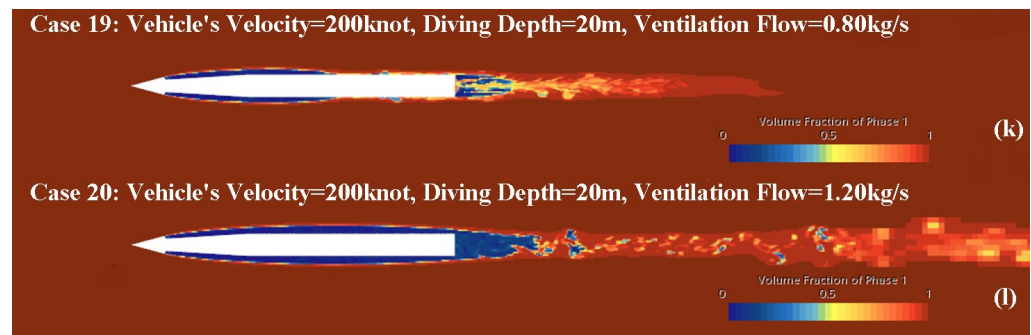


Figure 10. Cont.



**Figure 10.** Contour plots of the liquid phase volume fraction, where the ventilated cavitation occurs in the practical environment, including: (a) Case 8, (b) Case 9, (c) Case 10, (d) Case 11, (e) Case 12, (f) Case 13, (g) Case 14, (h) Case 15, (i) Case 16, (j) Case 17, (k) Case 19, (l) Case 20.



**Figure 11.** Contour plots of the volume fraction of the air composition for Case 18.

The spectrum diagram in Figure 12 indicates that regardless of the type of operating condition, the noise amplitude of the cavitation flow part after the cavitation phenomenon is always higher than the cone part. This issue confirms previous research that the cavitation flow is the main source of the hydrodynamic noise after the cavitation occurs. As for the characteristic frequency spectrum, as illustrated in Figure 12b,d, a clear characteristic peak is observed near 1 kHz in the ventilated cavitation condition, while there is no characteristic peak in Figure 12a,c. Therefore, we can infer that the noise characteristic frequency related to the pressure fluctuation caused by the ventilation and the fragmentation of the ventilated air in the wake are in this frequency range and will radiate to a higher frequency band. Then looking at Figure 12c,d, a noticeable noise characteristic peak is observed near 8 kHz, radiating widely and strongly. This characteristic peak is not evident in Figure 12a,b. Therefore, it is inferred that this characteristic peak is related to the pressure fluctuation caused by the incoming flow impacting the cavitator. Furthermore, several similar amplitude characteristic peaks are in the frequency range of 3 kHz to 10 kHz, which the evolution, pulsation, and shedding of the cavitation flow may cause. By comparing the noise under four different operating conditions in the frequency range of 10 to 40 kHz, the total hydrodynamic noise exhibits a decreasing trend, which indicates the absence of noise sources in this frequency range. In the frequency range of 40 to 80 kHz, there are characteristic peaks under natural cavitation conditions but no characteristic peaks under ventilated cavitation conditions. Considering the high background pressure in the flow field and the high potential energy in the bubble flow, it is inferred that this characteristic peak is related to the collapse of the bubble cluster and the propagation of pressure waves [18].

Regarding the order characteristics of the hydrodynamic noise of the vehicle after cavitation occurs, Tu et al. [13], Skidmore et al. [20], and Nouri et al. [23] have each presented results for their investigated conditions. This paper analyzes the characteristics of the hydrodynamic noise order of our vehicle model under several operating conditions.

As presented in Figure 13, the hydrodynamic noise exhibits monopole characteristics only when the vehicle speed is relatively low. Furthermore, as demonstrated in Figure 13b–d, the hydrodynamic noise exhibits dipole characteristics under ventilated cavitation or natural supercavitation conditions with high vehicle speed and background pressures, and the following content also supports this finding.



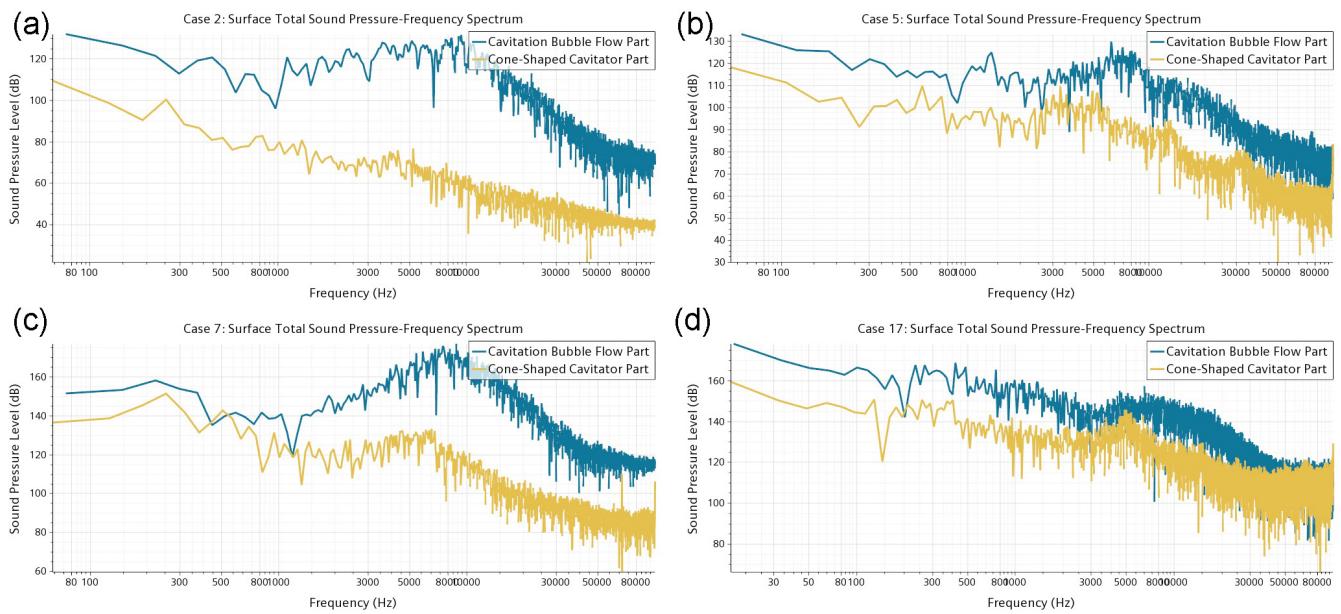


**Figure 12.** The total surface pressure–frequency spectrum of the cavitation flow part and the cone-shaped cavitator part under four distinct conditions, including: (a) Case 2: natural supercavitation in the experimental environment, (b) Case 5: ventilated supercavitation in the experimental environment, (c) Case 7: natural supercavitation in the practical environment, (d) Case 17: ventilated supercavitation in the practical environment.

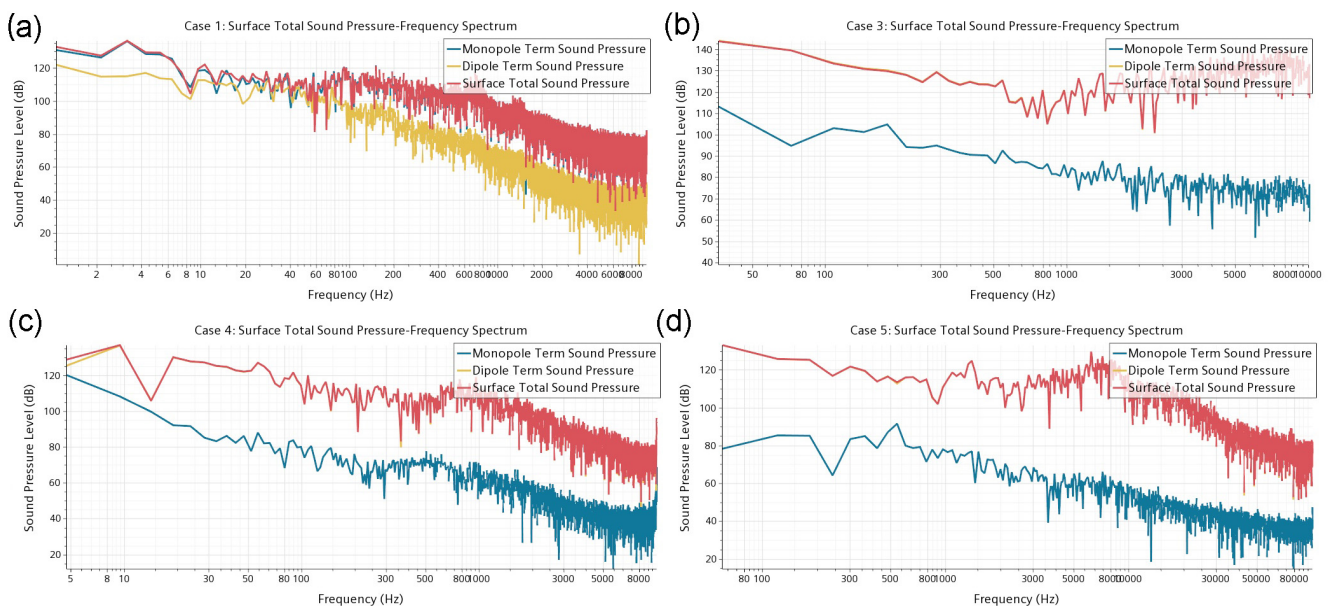


**Figure 13.** Surface total sound pressure–frequency spectrum of hydrodynamic noise of various orders in the experimental environment for several cases: (a) Case 1, (b) Case 3, (c) Case 4, (d) Case 5.

As shown in Figure 14, it can be seen that at high speed, pressure, and under ventilation condition, the noise consistently exhibits dipole characteristics. However, it is emphasized herein that in the low natural cavitation conditions, as illustrated in Figure 14a,b, the monopole sound cannot be ignored. This may be because the Mach number of the vehicle flow is low, which leads to the high sound efficiency of the monopole sound source.

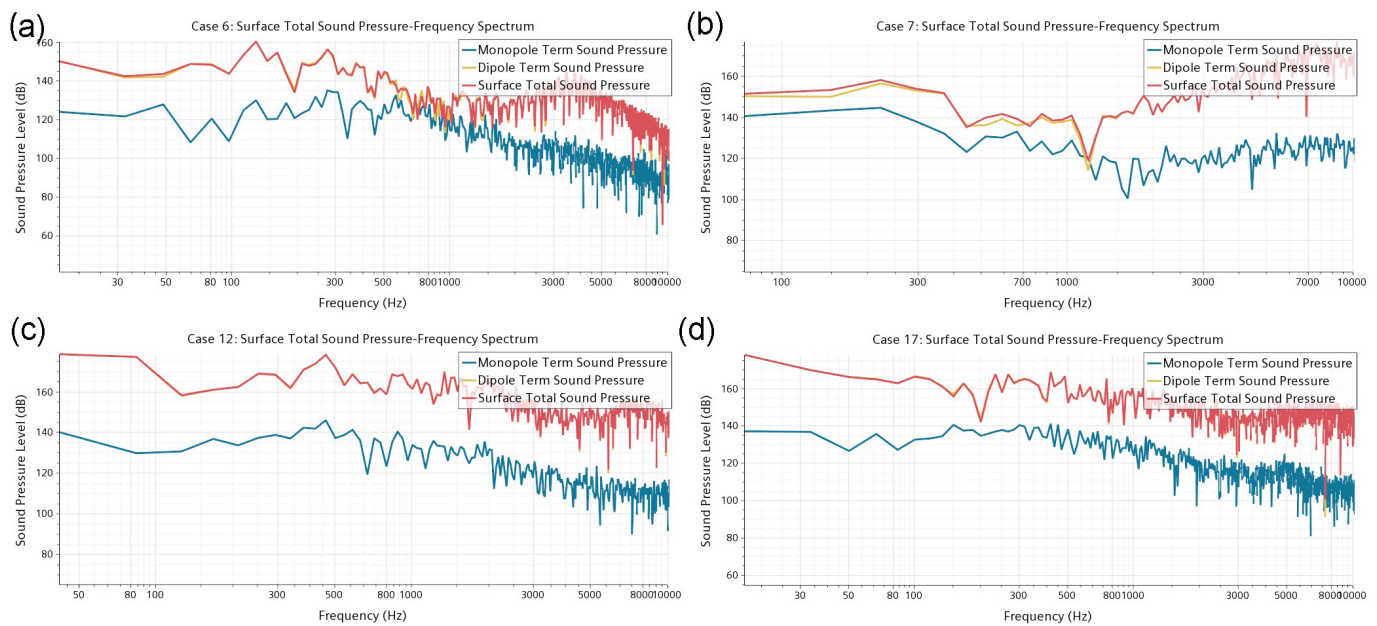


**Figure 14.** Surface total sound pressure–frequency spectrum of hydrodynamic noise of various orders in the practical environment for several cases: (a) Case 6, (b) Case 7, (c) Case 12, (d) Case 17.

#### 4.3. Hydrodynamic Noise under Different Operating Conditions

In practical applications, supercavitation vehicles usually travel in high-speed practical seas, and it is challenging to generate supercavitation in non-ventilated conditions. Therefore, this section focuses on cases where ventilated cavitation occurs in practical environments. In the following, we will no longer discuss separately the noise generated by the cone part, the cavitation flow part of the vehicle, and the different noise orders. Instead, we will focus on the influence of various operating conditions on the hydrodynamic noise of the vehicle. Firstly, we must investigate the effects of ventilation on noise characteristics. Based on Table 2, to ensure that the proportion and morphology of the liquid and gas phases are similar, we choose Case 6 and Case 12 for further comparison investigations. It should be noted here that the ventilation air is non-condensable, so there is a thin air film outside the main part of the ventilated cavitation in the ventilation condition.

As demonstrated in Figure 15, the total sound pressure on the vehicle surface under the ventilated cavitation condition is much higher than that under the natural cavitation condition in the entire frequency range. To ensure that the proportion and morphology of the liquid and gas phases are similar, the vehicle speed in the ventilated cavitation condition is lower than that in the natural cavitation condition. Moreover, higher flow generally corresponds to higher noise amplitudes. Therefore, it can be concluded that the hydrodynamic noise produced by the ventilated cavitation is much higher than that caused by natural cavitation when the situation of cavitation bubble flow and ventilated bubble flow is similar. This phenomenon may be related to the pressure fluctuations caused by ventilation near the vent and the fragmentation of ventilated air in the wake. Observing the characteristic frequency, there is a significant peak in flow noise in the natural cavitation condition in the frequency range between 3 to 5 kHz, and in the ventilated cavitation condition, this peak is shifted to a higher frequency between 5 to 8 kHz. The discrepancies between vapor and air components might cause this characteristic frequency difference.

In the second step, the effects of background pressure, vehicle speed, and ventilation flow on hydrodynamic noise are discussed separately. In studying the effect of the background pressure, it is necessary to control the ventilation flow and constant vehicle speed and ensure the presence of supercavitation. Referring to Table 4 and Figure 10, the hydrodynamic noise in the flow field of Case 11, Case 14, and Case 17 is comparable.



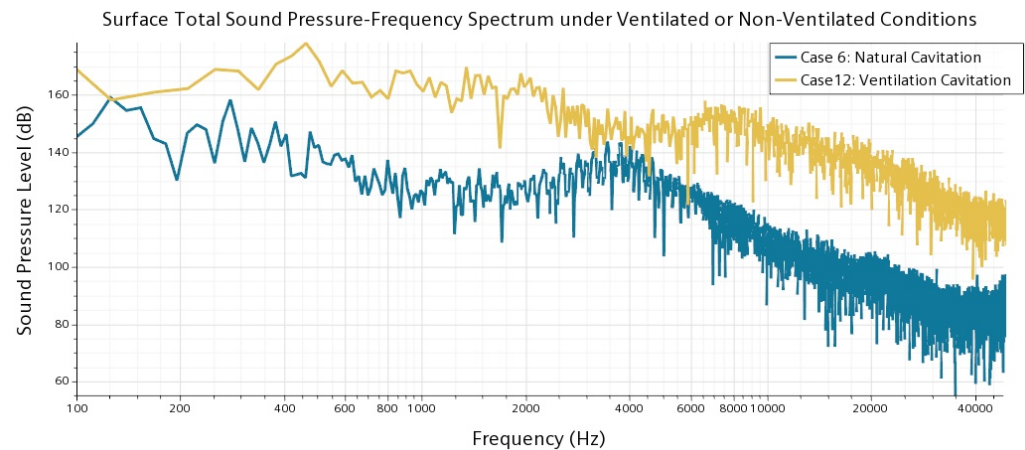


**Figure 15.** Surface total sound pressure–frequency spectrum of hydrodynamic noise under natural cavitation and ventilated cavitation conditions.

In Figure 16, in the frequency range of 1 and 3 kHz, the shallower the depth of water a vehicle navigates, the higher the amplitude of its noise. When the depth of water is shallow, larger-scale ventilated supercavitation flow’s pulsation and detachment cause higher noise. In the frequency interval of 3–8 kHz, on the one hand, the larger-scale ventilated supercavitation flow has a more substantial masking effect. On the other hand, larger-scale ventilated supercavitation flow pulsation and detachment cause higher noise, which makes it difficult to draw direct conclusions about the monotonic correlation between the diving depth and the noise amplitude in this frequency range. As for the characteristic spectrum, the shallower the diving depth the vehicle travels, the lower the characteristic peak frequency corresponding to the pulsations of the ventilated supercavitation flow. In the frequency range between 40 and 100 kHz, there is no characteristic peak related to the cavitation bubble collapse under ventilation conditions because the ventilated air is non-condensable, the low-frequency noise is difficult to radiate into this region, and the efficiency for the masking effect is low. Therefore, the noise generated by the supercavitation flow cannot be ignored, and increasing its scale increases the noise amplitude.

Then, in examining the effect of the vehicle speed, it is necessary to control the ventilation flow and constant diving depth and ensure the existence of ventilated supercavitation. Referring to Table 4 and Figure 11, the hydrodynamic noise in the flow fields of Case 9, Case 17, and Case 20 can be selected for comparison.

As shown in Figure 17, the noise amplitude of Case 20 is much higher than that of Case 17 and Case 9 in the frequency range of 1–8 kHz. It is because, in Case 20, the smaller scale of the supercavitation flow weakens the masking effect of the low-frequency noise and the higher inflow velocity leads to higher noise, which is related to the pressure fluctuation caused by the inflow impact. The noise amplitudes of Case 9 and Case 17 are similar. It might be because the supercavitation flow pulsation in Case 9 is stronger than that in Case 17, the pressure fluctuation caused by the inflow impact in Case 9 is weaker than that in Case 17, and the masking effect of the ventilated supercavitation flow in Case 9 is stronger than that in Case 17. These factors jointly lead to the absence of a uniform correlation between the vehicle speed and the noise amplitude when the vehicle’s velocity is in the range of 160 to 180 knots. Furthermore, in the frequency range of 3 to 8 kHz, the faster the vehicle’s velocity, the lower the frequency at which the characteristic peak of the noise spectrum appears. It can be concluded that the characteristic frequency peak of the supercavitation flow’s pulsation is essentially affected by the scale of the ventilated supercavitation flow. The larger the scale of the supercavitation flow, the closer the characteristic peak to the low frequency range. In the frequency range of 40 to 100 kHz, the hydrodynamic noise amplitude under the high vehicle velocity condition is higher than that under the low vehicle velocity condition. The analysis shows that the noise in this

frequency range is strongly correlated with the background noise in the flow field. When the inflow velocity is higher, the background noise in the flow field is stronger.

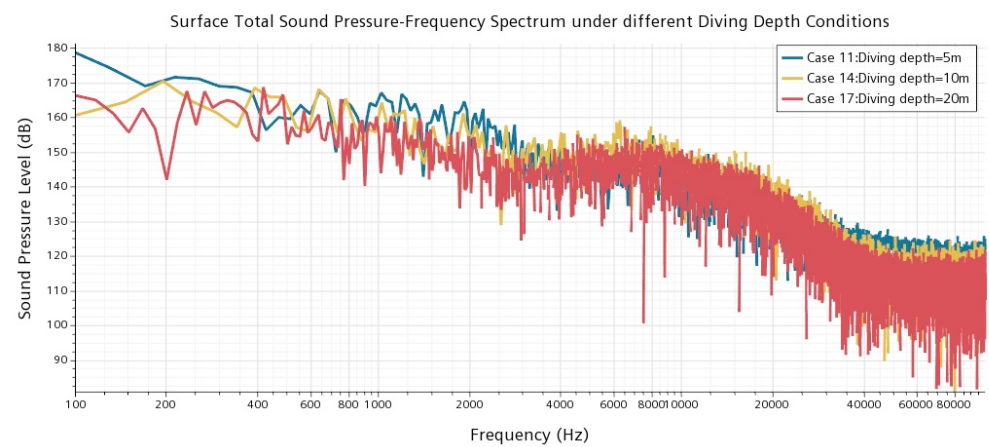


**Figure 16.** Surface total sound pressure–frequency spectrum of the hydrodynamic noise under different diving depth conditions for several cases: Case 11: diving depth = 5 m, Case 14: diving depth = 15 m, and Case 17: diving depth = 20 m).

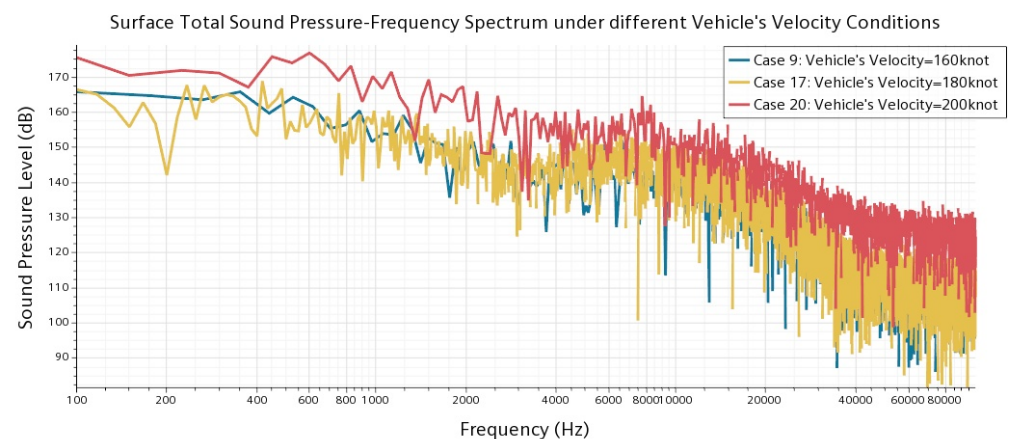


**Figure 17.** Surface total sound pressure–frequency spectrum of hydrodynamic noise under different vehicle velocity conditions for several cases: Case 9: vehicle's velocity = 160 knot, Case 17: vehicle's velocity = 180 knot, and Case 20: vehicle's velocity = 200 knot).

Unlike explorations that investigate the effects of vehicle velocity or background pressure on the hydrodynamic noise of supercavitation, the following paragraph deals with the effect of ventilation flow on noise. By adjusting the ventilation flow, this study aims to investigate the differences in the noise produced by the air film and the complete supercavitation structure.

As shown in Figure 18, the effect of ventilation flow on the hydrodynamic noise is quite complex. Firstly, ventilation causes pressure fluctuations, so as the ventilation flow rate increases, the noise amplitude near 1 kHz will significantly increase. Secondly, the ventilation flow rate is a decisive factor that affects the scale of ventilated cavitation flow on the vehicle's surface, and the scale of ventilated cavitation flow can affect both its masking effect to noise and its own fluctuation and shedding. Compared with the case without supercavitation, the noise amplitude near 8 kHz significantly decreases after the ventilation supercavitation occurs. In addition, under different ventilation conditions, whether the ventilated supercavitation will occur, the noise amplitude shows a clear downward trend from 8 to 40 kHz and is similar between 40 and 100 kHz. After the occurrence of ventilation supercavitation, the noise spectrum does not change between 8 and 100 kHz significantly when increasing the ventilation flow rate again, which is

inconsistent with the above caused by controlling the sailing depth or background pressure.

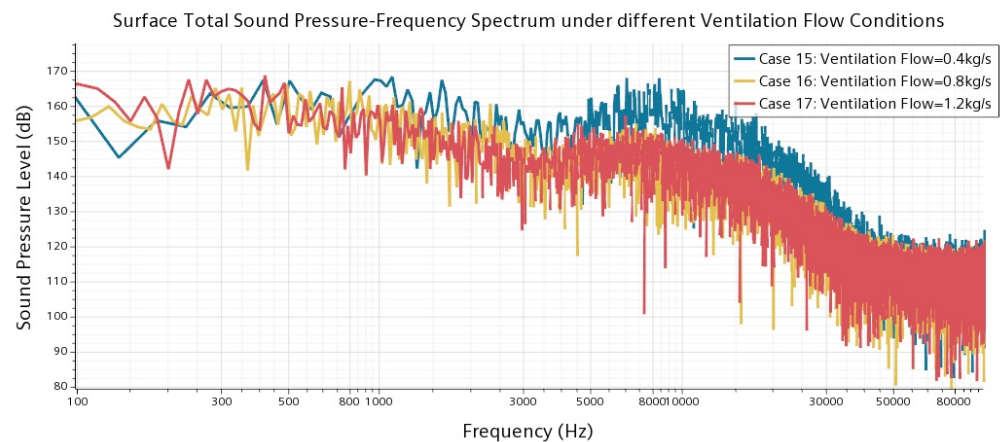


**Figure 18.** Surface total sound pressure–frequency spectrum of hydrodynamic noise under various vehicle velocities, including Case 15: ventilation flow = 0.4 kg/s, Case 16: ventilation flow = 0.8 kg/s, and Case 17: ventilation flow = 1.2 kg/s).

This confirms the conjecture about the effect of the sailing depth and background pressure on the noise amplitude over the entire frequency range. Regarding the fluctuation and shedding of ventilation cavitation flow, the longer the length of the ventilation cavitation flow, the closer the characteristic peak caused by the cavitation flow fluctuation in the frequency range of 3–8 kHz to the low-frequency band. At the same time, although high ventilation flow rates can cause higher pressure fluctuations and larger ventilated cavitation flow shedding, their contributions to noise compared to the supercavitation flow’s masking effect are relatively small. Therefore, the noise amplitude in the 1–8 kHz frequency range is relatively low under high ventilation flow. In summary, multiple cases under ventilation conditions exhibit common characteristics in their spectral features, but also demonstrate significant differences. The commonalities are mainly manifested in the presence of a distinctive peak near 8 kHz and a general decrease in the spectrum between 8 and 40 kHz. The differences primarily lie in the characteristic frequencies and noise amplitudes between 1 and 10 kHz. These commonalities and differences are closely related to the velocity of the inflow, physical properties of the background flow field, and the scale of cavitation on the vehicle’s surface. This paper extensively explores these contents.

## 5. Conclusions

This paper presents numerical simulations of the flow and acoustic fields surrounding an underwater supercavitation vehicle. Under ventilation conditions, three representative cavitation phenomena: air film, critical supercavitation, and complete supercavitation structure are identified. We examine the effects of operating conditions on the cavitation phenomenon. A complete supercavitation structure requires three times more ventilation flow than the air film. Low vehicle speed could reduce the threshold of ventilated supercavitation, and low background pressure will reduce the stability of the supercavitation structure. So when studying and applying ventilated supercavitation technology, it is important to maintain a relatively high value of the natural cavitation number, with  $\sigma > 5 \times 10^{-2}$  offering a suitable range.

Then we investigated the feature spectrum, corresponding noise source, and order characteristics of hydrodynamic noise. Under the ventilated cavitation condition, several characteristic peaks are created by the flow and fragmentation of the ventilated air near the frequency range of 1 kHz. In all operating conditions, the cavitation flow pulsation causes multiple characteristic peaks between 3 and 10 kHz, and the pressure fluctuation caused by the impact of incoming flow forms a prominent characteristic peak near 8 kHz. The noise amplitude reveals a significant reduction in the range between 10 and 40 kHz.

Under natural cavitation conditions, the collapse of bubble clusters produces a characteristic peak between 40 and 80 kHz. Regarding the characteristics of the noise order, for the vehicle model used in our study, only when the vehicle speed is less than 10 m/s, the hydrodynamic noise exhibits a monopole dominated behavior. In other conditions, the hydrodynamic noise of the vehicle shows a dipole dominated behavior.

The effect of operating conditions on hydrodynamic noise is methodically assessed. The shielding effect is due to the obstruction of noise propagation by the supercavitation flow. Meanwhile, the vehicle speed and background pressure affect the hydrodynamic noise of the ventilated supercavitation flow by influencing its scale. As the scale of the supercavitation flow rises, the noise amplitude near 1 kHz significantly grows, and the noise amplitude between 3 and 10 kHz first increases and then decreases. In addition, the characteristic peaks produced by supercavitation flow fluctuations are shifted to a lower frequency under ventilation conditions.

In general, the novelty of our work lies in the comprehensive study of the influence of various operating conditions on the ventilated cavitation phenomenon and the noise characteristic spectrum in a wide frequency domain. In future research, we plan to explore the reliability of our numerical results by testing different vehicle models. Moreover, guided by the numerical study, we will conduct experimental research considering the noise generated by the ventilation jet and propellers.

**Author Contributions:** Conceptualization, J.Y., J.Z. and Y.W.; methodology, J.Y. and J.Z.; software, J.Y.; validation, J.Y. and J.Z.; investigation, J.Y.; resources, J.Z. and Y.W.; data curation, J.Y.; writing—original draft preparation, J.Y.; writing—review and editing, J.Z.; supervision, J.Z. and Y.W.; project administration, Y.W. and P.Z.; funding acquisition, Y.W. and P.Z. All authors have read and agreed to the published version of the manuscript.

**Funding:** This research was funded by National Key R&D Program of China (2022YFF0607505) and Zhejiang provincial natural science foundation (LQ21A020006); The APC was funded by National Key R&D Program of China (2022YFF0607505) and Zhejiang provincial natural science foundation (LQ21A020006).

**Institutional Review Board Statement:** Not applicable.

**Informed Consent Statement:** Not applicable.

**Data Availability Statement:** Not applicable.

**Conflicts of Interest:** The authors declare no conflict of interest.

## Abbreviations

The following abbreviations are used in this manuscript:

LES	Large Eddy Simulation
VOF	Volume of Fluid
FFT	Fast Fourier Transform

## References

1. Hrubes, J. High-speed imaging of supercavitating underwater projectiles. *Exp. Fluids* **2001**, *30*, 57–64. [\[CrossRef\]](#)
2. Knapp, R.; Daily, J.; Hammitt, F. *Cavitation*; Eng. Soc. Monographs; McGraw-Hill: New York, NY, USA, 1970; Volume 39, p. 213.
3. Varga, J.; Sebestyen, G. Experimental investigation of cavitation noise. *Houille Blanche* **1966**, *8*, 905–910. [\[CrossRef\]](#)
4. De, M.; Hammitt, F. New method for monitoring and correlating cavitation noise to erosion capability. *J. Fluids Eng.* **1982**, *104*, 434–441. [\[CrossRef\]](#)
5. Liu, X.; Song, J.; Li, B.; He, J.; Zhang, Y.; Li, W.; Xie, F. Experimental study on unsteady characteristics of the transient cavitation flow. *Flow Meas. Instrum.* **2021**, *80*, 102008. [\[CrossRef\]](#)
6. Rabiee, A.; Alishahi, M.; Emdad, H.; Saranjam, B. Part A: Experimental investigation of unsteady supercavitating flows. *Iran. J. Sci. Technol. Trans. Mech. Eng.* **2011**, *104*, 15–29.
7. May, A. Water entry and the cavity-running behavior of missiles. In *Technical Report, Navsea Hydroballistics Advisory Committee Silver*; Springer: Berlin/Heidelberg, Germany, 1975.



8. Savchenko, Y.N. *Supercavitating Object Propulsion*; Technical Report; Krainian Academy of Sciences Kiev Inst of Hydromechanics: Brussels, Belgium, 2001.
9. Jiang, Y.; Jeong, S.W.; Ahn, B.K.; Kim, H.T.; Jung, Y.R. Experimental investigation of drag characteristics of ventilated supercavitating vehicles with different body shapes. *Phys. Fluids* **2019**, *31*, 052106. [\[CrossRef\]](#)
10. Mohammadrahimi, A.; Negahdari, M.; Hosseini, S.A.; Parsaei, E. Investigation of the shape of the torpedo nose in supercavitation and numerical analysis of the effect of gas injection. *J. Mar. Sci. Technol.* **2021**. Available online: [https://jmst.kmsu.ac.ir/article\\_130211.html?lang=en](https://jmst.kmsu.ac.ir/article_130211.html?lang=en) (accessed on 1 March 2023).
11. Shao, S.; Balakrishna, A.; Yoon, K.; Li, J.; Liu, Y.; Hong, J. Effect of mounting strut and cavitator shape on the ventilation demand for ventilated supercavitation. *Exp. Therm. Fluid Sci.* **2020**, *118*, 110173. [\[CrossRef\]](#)
12. Pham, V.D.; Hong, J.W.; Hilo, A.K.; Kim, K.; Ahn, B.K. Experimental investigation of ventilated supercavitation behind cone-shaped with different angles and disk-shaped cavitators. *Int. J. Nav. Archit. Ocean Eng.* **2022**, *14*, 100477. [\[CrossRef\]](#)
13. Tu, J.; Gan, L.; Ma, S.; Zhang, H. Flow noise characteristics analysis of underwater high-speed vehicle based on LES/FW-H coupling model. *Acoust. Aust.* **2019**, *47*, 91–104. [\[CrossRef\]](#)
14. Ramesh, S.S.; Lim, K.M.; Zheng, J.; Khoo, B.C. Numerical analysis of flow induced noise propagation in supercavitating vehicles at subsonic speeds. *J. Acoust. Soc. Am.* **2014**, *135*, 1752–1763. [\[CrossRef\]](#) [\[PubMed\]](#)
15. Ho, S.A.; Howe, M.; Salton, A. Low frequency sound produced by a ventilated supercavitating vehicle. *J. Sound Vib.* **2011**, *330*, 1634–1643. [\[CrossRef\]](#)
16. Gilbert, J.; Howe, M.; Koch, R. On sound generated by gas-jet impingement on a bubbly gas–water interface, with application to supercavity self-noise. *J. Sound Vib.* **2012**, *331*, 4438–4447. [\[CrossRef\]](#)
17. Zhang, L.; Zhang, J.; Deng, J. Numerical investigation on the collapse of a bubble cluster near a solid wall. *Phys. Rev. E* **2019**, *99*, 043108. [\[CrossRef\]](#)
18. Zhang, J.; Zhang, L.; Deng, J. Numerical study of the collapse of multiple bubbles and the energy conversion during bubble collapse. *Water* **2019**, *11*, 247. [\[CrossRef\]](#)
19. Zhang, F.Z.; Li, G.J.; Hu, W.S.; Mu, L. Modeling and Simulation of Cavitation Noise of Supercavitating Vehicle. Available online: <https://dpi-journals.com/index.php/dtcse/article/view/23664> (accessed on 1 March 2023).
20. Skidmore, G.M.; Brungart, T.A.; Lindau, J.W.; Moeny, M.J. Noise generated by ventilated supercavities. *Noise Control Eng. J.* **2015**, *63*, 94–101. [\[CrossRef\]](#)
21. Skidmore, G.M.; Brungart, T.A.; Lindau, J.W.; Moeny, M.J. The control of ventilated supercavity pulsation and noise. *Int. J. Multiph. Flow* **2016**, *85*, 14–22. [\[CrossRef\]](#)
22. Yasui, K. Origin of the broad-band noise in acoustic cavitation. *Ultrason. Sonochem.* **2022**, *93*, 106276. [\[CrossRef\]](#)
23. Nouri, N.M.; Riahi, M.; Valipour, A.; Raeyatpishe, M.M.; Molavi, E. Analytical and experimental study of hydrodynamic and hydroacoustic effects of air injection flow rate in ventilated supercavitation. *Ocean Eng.* **2015**, *95*, 94–105. [\[CrossRef\]](#)
24. Hirt, C.W.; Nichols, B.D. Volume of fluid (VOF) method for the dynamics of free boundaries. *J. Comput. Phys.* **1981**, *39*, 201–225. [\[CrossRef\]](#)
25. Sauer, J. *Instationaer Kavitierende Stroemungen-Ein Neues Modell, Basierend auf Front Capturing VOF und Blasendynamik*, Ph.D. Dissertation, Universitaet Karlsruhe, Karlsruhe, Germany, 2000.
26. Spurk, J. On the gas loss from ventilated supercavities. *Acta Mech.* **2002**, *155*, 125–135. [\[CrossRef\]](#)

**Disclaimer/Publisher’s Note:** The statements, opinions and data contained in all publications are solely those of the individual author(s) and contributor(s) and not of MDPI and/or the editor(s). MDPI and/or the editor(s) disclaim responsibility for any injury to people or property resulting from any ideas, methods, instructions or products referred to in the content.